A Target-Attenuation and Mask-Purification Network for Hyperspectral Anomaly Detection

Ke Wu
Instrument Science and Optoelectronic Engineering
Nanchang Hangkong University
Nanchang, China
wuke0801@163.com

Song Liu*
Instrument Science and Optoelectronic Engineering
Nanchang Hangkong University
Nanchang, China
liusong@nchu.edu.cn

Congxuan Zhang*
Instrument Science and Optoelectronic Engineering
Nanchang Hangkong University
Nanchang, China
zcxdsg@163.com

Zhen Chen
Instrument Science and Optoelectronic Engineering
Nanchang Hangkong University
Nanchang, China
dr_chenzhen@163.com

***Abstract*—Hyperspectral anomaly detection (HAD) aims to identify targets with spectral characteristics distinct from the background. Reconstruction-based methods are commonly used and effective in HAD, but they are susceptible to the influence of anomalous targets during background generation, which can compromise the purity of the background and reduce detection performance. To address this issue, we propose the Target-Attenuation and Mask-Purification Network (TAMP-Net). Our framework first employs a pre-detection module for initial target localization, followed by a decaying background replacement strategy to attenuate the influence of anomalies. Subsequently, a high-ratio masked autoencoder is employed, applying random masking to the remaining regions to further purify the background. Finally, the anomaly map is generated by computing the residual between the original image and the reconstructed background. Experiments conducted on multiple hyperspectral datasets have demonstrated the effectiveness and superiority of the proposed method. Our source code and datasets are publicly available at: https://github.com/orglye/TAMP-Net.**

***Index Terms*—Hyperspectral images, Anomaly detection, Mask autoencoder, Deep learning**

I. Introduction

Hyperspectral images (HSIs) provide spatial context and per-pixel spectra, enabling precise material discrimination [1]–[3]. Hyperspectral anomaly detection (HAD) seeks targets spectrally distinct from background without prior target signatures [4], and is used in agriculture, reconnaissance, environmental, and mineral exploration [5], [6].

Traditional approaches include statistics-based methods like RX [7], which uses Mahalanobis distance. Representation-based detectors such as collaborative representation [8] and decomposition-based techniques like low-rank and sparse matrix decomposition [9] to separate background and anomalies. In recent years, convolutional neural networks (CNNs) have demonstrated excellent capabilities in extracting discriminative spectral-spatial features from HSIs [10]–[12], thereby improving anomaly detection performance. However, they remain limited in modeling complex data distributions. To address this, generative adversarial networks (GANs) have been introduced for hyperspectral analysis [13], as they can more effectively model the background data distribution and achieve more accurate anomaly separation. Current mainstream methods predominantly rely on reconstruction strategies, typically using autoencoders or GANs under the assumption that backgrounds can be accurately reconstructed while anomalies cannot [14]–[16]. Nevertheless, these approaches are susceptible to contamination from anomalous pixels, and erroneous reconstruction of such pixels during training can bias background estimation and degrade detection accuracy. Although reconstruction-based methods such as BS^{3}LNet [17] mitigate this issue by masking center pixels and predicting them from the surrounding context, their performance remains limited when dealing with large anomalous targets. NL2Net [18] innovatively employs a dual-branch architecture and pixel-shuffle downsampling strategy to alleviate large-scale anomaly interference, yet it still faces challenges including high computational complexity, reliance on manual parameter tuning, and limited adaptability to complex scenes or small/dense anomalies.

To solve the above problem, we propose a unified purification network that integrates decaying background replacement with a masked autoencoder, achieving target suppression and background purification. Initial anomaly localization is performed using parallel statistical detectors. Subsequently, a background replacement strategy is applied, which utilizes spectral angle histogram binning and Chebyshev distance weighting [19] to achieve smooth pixel substitution. Following this, the purified background is then reconstructed using a masked autoencoder to suppress residual contamination.

This work was supported in part by the National Natural Science Foundation of China (Grant Nos. U25A20480, 62401243, and U2441241), and the Jiangxi Province Natural Science Foundation (Grant Nos. 20253BAC280056, 20242BAB20038, and 20252BAC240010).

Congxuan Zhang and Song Liu are the corresponding authors.

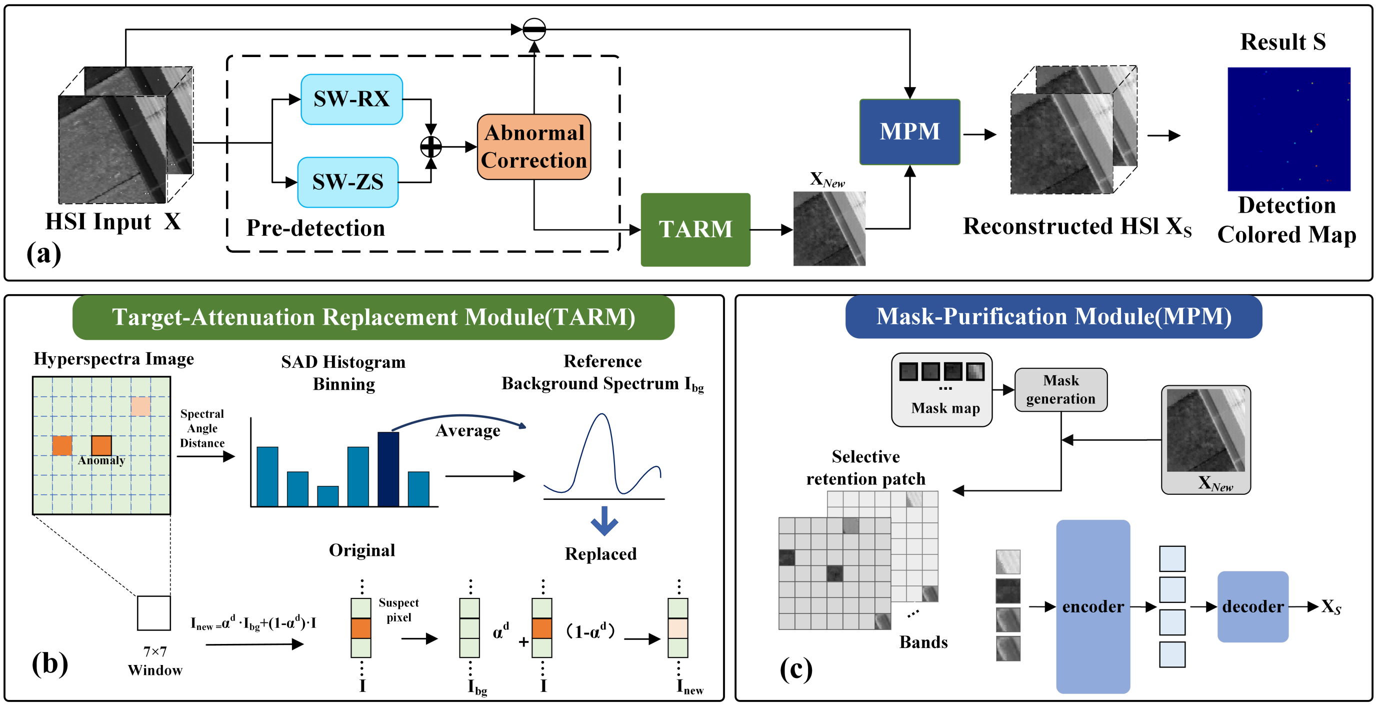

Fig. 1. Framework of the proposed TAMP-Net for HAD.

Finally, anomalies are detected by computing the residual between the original input and the reconstructed image. The contributions of this work can be summarized as follows:

1) To reduce the interference of the target on the background, a collaborative framework combining target attenuation replacement with a mask autoencoder is proposed for gradual background purification.

2) An adaptive background optimization strategy based on spectral angle and Chebyshev distances is designed, enhancing the accuracy and smoothness of background reconstruction.

3) We introduce a masking mechanism to dynamically suppress undetected anomalies, thereby reducing influence from missed targets and enhancing detection accuracy.

II. Methodology

The framework of Target-Attenuation and Mask-Purification Network (TAMP-Net) is shown in in Fig. 1 (a). The preprocessing generates an anomaly-focused graph, then replaces the pre-detection target with a locally attenuated background. Next, a high mask rate encoder reconstructs the clean background. Finally, the residuals between the original image and the reconstructed background are used to detect anomalies.

A. Pre-detection Module

The Pre-detection Module aims to quickly identify abnormal targets and replace their spectra with typical background spectra, thereby initially purifying the background area and providing a relatively clean input for subsequent reconstruction.

In the pre-detection module, we adopt a parallel-path scheme to rapidly locate multi-scale anomalies by combining two sliding-window detectors: a Sliding-Window RX (SW-RX) and a Sliding-Window Z-Score (SW-ZS). For SW-RX, the RX score is computed per pixel within a local window. For SW-ZS, each spectral band is locally Z-normalized and bandwise scores are aggregated to form a comprehensive Z-score map. The two score maps are first normalized and fused at the score level. Subsequently, binarization is performed, where pixels with scores exceeding a predefined threshold are converted to the foreground (anomaly candidates) to generate initial candidate regions. To reduce the impact of initial anomaly localization errors on subsequent processing,we use geometric constraints to suppress false positives and ensure that most potential anomalies are retained. Connected components are extracted, and the aspect ratios of their minimum bounding rectangles are computed. Regions with $\max(\frac{w}{h},\frac{h}{w})>3$ are considered elongated background structures (e.g., roads or bridges) and subsequently removed. These steps refine the residual artifacts to generate a purified preliminary detection result.

B. Target-Attenuation Replacement Module

To effectively suppress contaminated anomalous pixels and ensure smooth spectral transitions, we propose a Target-Attenuation Replacement Module (TARM) as the first purification stage in the TAMP-Net, as shown in Fig. 1 (b).

For each pixel identified as an anomaly, a local window of size 7×7 is constructed around it. Taking the spectrum of the central pixel as the reference, the spectral angle distances (SAD) [20], [21] between the center and its neighboring pixels are calculated. These SAD values are then statistically grouped

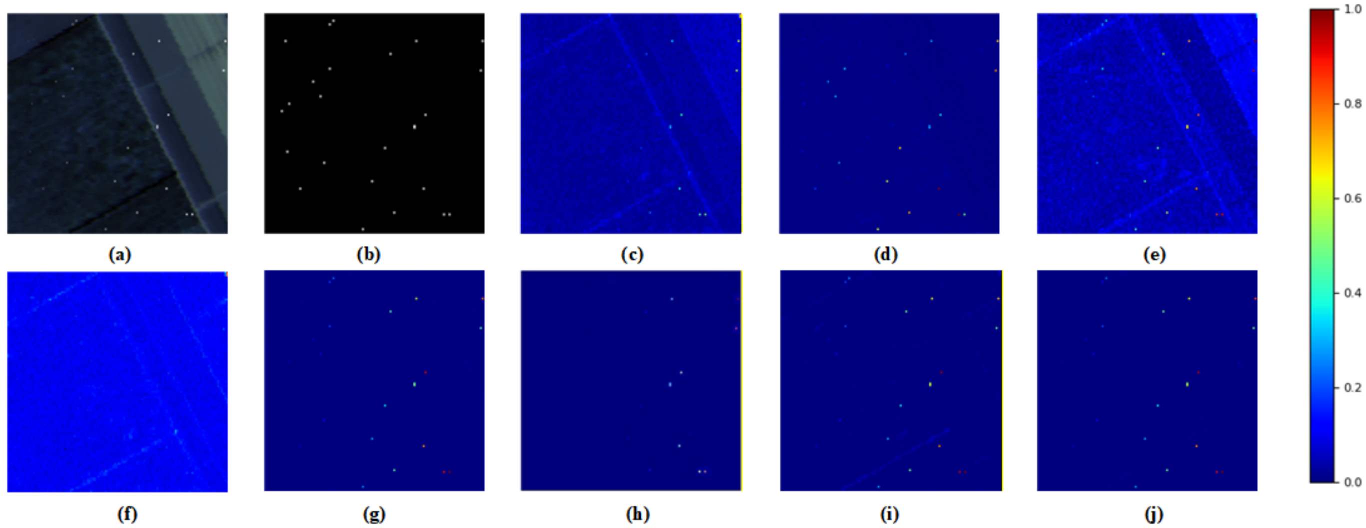

Fig. 2. Detection maps of different methods on Salinas dataset. (a) Pseudocolor image. (b) Ground truth. (c) RX. (d) CRD. (e) LRASR. (f) LSDM-Mog (g) BS^{3}LNet. (h) STAD. (i) NL2Net. (j) Ours.

into a fixed set of 10 equidistant histogram bins over the range [0, π]. The bin with the highest frequency is identified as representing the "typical background" range of SAD values. The spectra of all the neighboring pixels within this interval are averaged to obtain a representative background spectrum vector $\boldsymbol{I}_{bg}$, which is used to directly replace the spectrum of the central abnormal pixel. To achieve smooth spectral fusion and reduce possible residual anomalies, an attenuation fusion strategy was adopted to process pixels in adjacent suspicious pixels that were not marked as abnormal and whose SAD values were lower than the threshold. Each pixel in the neighborhood is assigned a decaying weight based on its Chebyshev distance d from the central pixel. The attenuation substitution process is:

$$\boldsymbol{I}_{new} = \alpha^d \cdot \boldsymbol{I}_{bg} + (1 - \alpha^d) \cdot \boldsymbol{I} \tag{1}$$

where, $\boldsymbol{I}$ represents the original spectrum. This weight determines the fusion ratio between the pixel's original spectrum and the typical background spectrum. Consequently, pixels in the central region exhibit more dominant background characteristics, while those farther from the center retain more of their original features.

C. Mask-Purification Module

Although the initial anomaly replacement has effectively addressed most salient anomalies, some regions may still contain residual or undetected anomalies. To further enhance the purity and consistency of background representation, the proposed method introduces a Mask-Purification Module (MPM), as shown in Fig. 1 (c), which employs a mask-guided background reconstruction mechanism.

This mechanism utilizes a vision Transformer-based [22]masked autoencoder that takes the preliminarily purified background image as input. By applying a high masking ratio (up to 90%) to the unreplaced regions, the model relies on only 10% of the reserved image patches to achieve image reconstruction via an encoder–decoder architecture. The model is optimized by minimizing the mean squared error between the reconstructed image and the initial background image $\boldsymbol{X}_{new}$. This approach compels the model to learn to infer global background structures from limited contextual information, significantly enhancing its capability for background modeling. Meanwhile, the high masking ratio effectively removes potential anomalous targets, thereby suppressing interference from anomalous signals. Finally, the purified reconstructed background is compared with the original input image via subtraction to produce a residual map that highlights the anomalous targets.

$$\boldsymbol{S} = \|\boldsymbol{X} - \boldsymbol{X}_S\| \tag{2}$$

III. EXPERIMENT RESULTS

A. Datasets

Three publicly available hyperspectral datasets were employed in this experiment: The Salinas dataset [23] is acquired by the AVIRIS-II sensor, retaining 204 valid bands after excluding 20 disturbed bands, with a spatial resolution of 3.3 m. Its anomalous targets correspond to man-made structures. The Urban dataset [24] is captured by the Hyperspectral Digital Image Acquisition Experiment (HYDICE) sensor, which has a spatial dimension of 80×100 pixels, a spatial resolution of 1 m, and 175 spectral bands in total. Its anomalous targets are small-scale urban facilities (e.g., vehicles, temporary installations). The Gulfport subset of the ABU (Airport-Beach-Urban) dataset [25] is obtained by the NASA AVIRIS sensor, which focuses on the airport and its surrounding areas, where the anomalous targets are aircraft with various scales.

B. Comparison Algorithms and Evaluation Metrics

1) Comparison Algorithms: To comprehensively evaluate the performance of the proposed method, we selected a variety

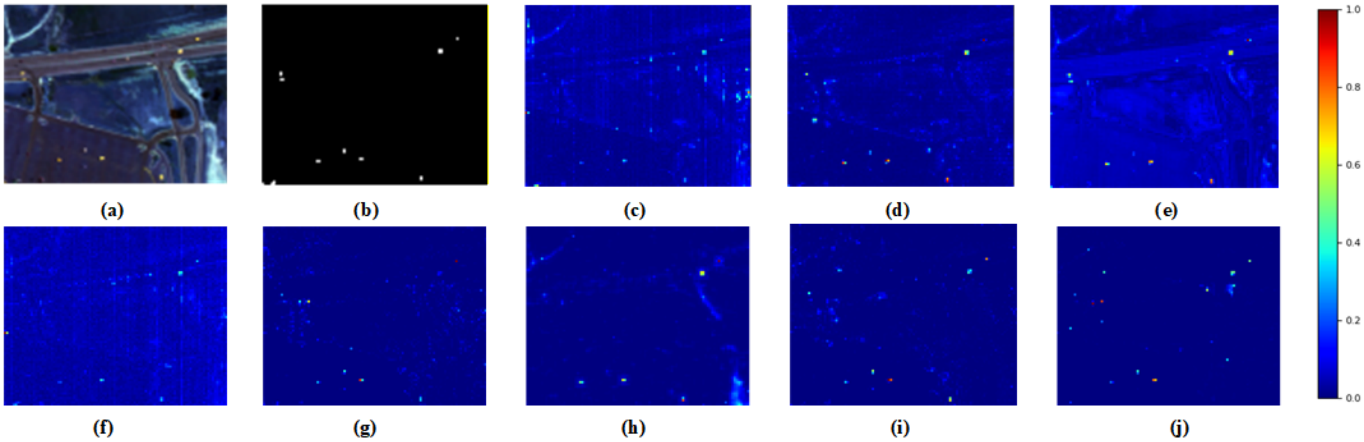

Fig. 3. Detection maps of different methods on HYDICE dataset. (a) Pseudocolor image. (b) Ground truth. (c) RX. (d) CRD. (e) LRASR. (f) LSDM-Mog (g) BS^{3}LNet. (h) STAD. (i) NL2Net. (j) Ours.

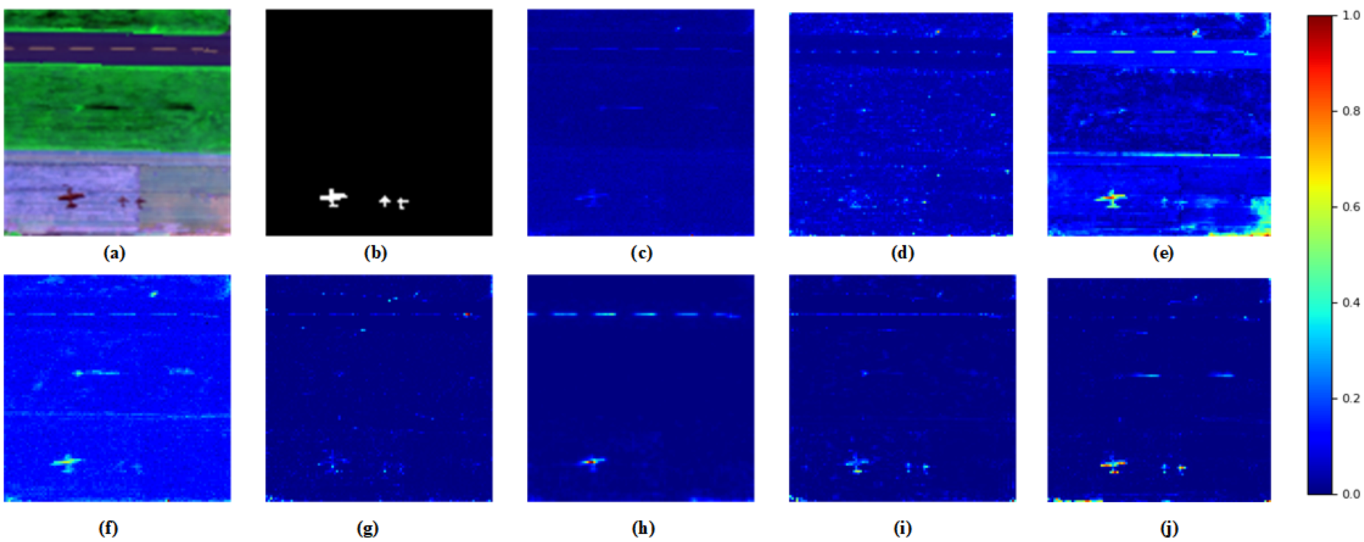

Fig. 4. Detection maps of different methods on Gulfport dataset. (a) Pseudocolor image. (b) Ground truth. (c) RX. (d) CRD. (e) LRASR. (f) LSDM-Mog (g) BS^{3}LNet. (h) STAD. (i) NL2Net. (j) Ours.

of representative hyperspectral anomaly detection algorithms for comparison. These algorithms cover different detection principles and techniques, as follows: the classic RX [7] algorithm based on statistics, two representation-based methods CRD [8] and LSDM-MoG [26], the decomposition-based method LRASR [9], and the deep learning-based methods including BS^{3}LNet [17], the newly proposed STAD [27] method, and the novel nonlocal and local feature-coupled self-supervised network (NL2Net) [18].

2) Evaluation Metrics: To assess the performance of representative comparative detectors, we adopted two commonly used metrics: the Receiver Operating Characteristic (ROC) [28] curve and the Area Under the ROC Curve (AUC). The ROC curve captures the trade-off between recall and false positive rate; the AUC serves as a quantitative measure of overall performance. A high-performing detector typically exhibits an ROC curve close to the top-left corner with an AUC near 1.0.

To further clarify performance differences between competing methods, we adjusted the ROC coordinate system to a logarithmic scale. In HAD, state of the art algorithms often yield near 1.0 AUC values, which compress curve differences in the critical low false alarm rate region under linear scaling and hinder intuitive discrimination of model superiority. Thus, logarithmic coordinates were used to magnify subtle performance gaps in this key region, enabling more accurate and discriminative comparison of each algorithm's detection capability.

C. Experimental Setup

TAMP-Net is implemented in PyTorch and optimized with AdamW for 6000 epochs using an initial learning rate of 1×10^{-4}, a cosine annealing schedule, and a batch size of 1. In preprocessing, both the SW-RX module and the SW-

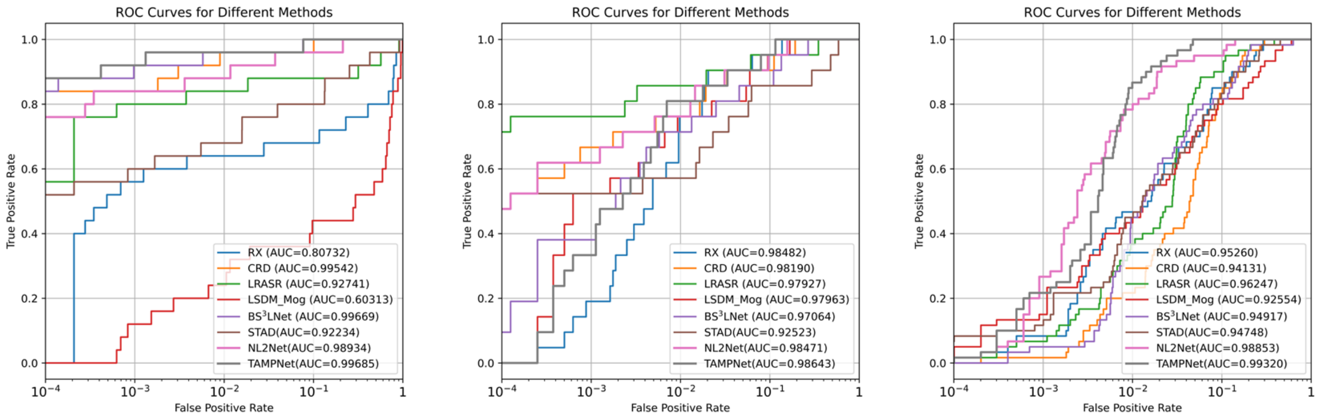

(a) **(b)** **(c)**

Fig. 5. ROC curves obtained by different methods for three datasets, where the horizontal axis is on a logarithmic scale. (a) Salinas dataset. (b) HYDICE dataset. (c) Gulfport dataset.

ZS module employ a 30×30 sliding window. The step size of the SW-RX module is 10, and the binary threshold is 20. In the TARM, we apply a 7×7 neighborhood, SAD threshold = 0.1, and decay factor α = 0.9. MPM is a mask autoencoder with a 12-layer Transformer encoder and a 4-layer decoder (embedding 192, 3 heads).

D. Experimental Results and Analysis

Figs. 2 3 4 present the colorized results of HAD achieved by 8 methods on the three considered datasets, where the first one in each figure is the pseudocolor hyperspectral image, the second one represents the ground truth of the detected anomalous targets, and the rest illustrate the result maps generated by different detectors.

Overall, TAMP-Net effectively suppresses anomalous background clutter while enhancing the contrast of anomalous objects, achieving the best AUC among all competing methods. On the Salinas dataset, RX and LSDM-Mog suffer from texture-induced false alarms, whereas CRD and BS^{3}LNet tend to over-suppress and consequently miss targets. Statistical methods like GRX and LRASR struggle with complex texture scenes due to their reliance on predefined probability distribution assumptions, while deep learning methods such as BS^{3}LNet and Auto-AD, despite optimizing background suppression, lack sufficient response to weak-signal targets. In contrast, TAMP-Net achieves a more ideal balance between background suppression and target retention.

On the Gulfport dataset, TAMP-Net demonstrates significantly superior detection performance compared to other algorithms, including NL2Net (which fuses local and nonlocal features via a dual-branch architecture, achieving an AUC of 0.9885 on the Gulfport dataset), exhibiting a clearer distinction between target and background regions. This improvement suggests that the TARM and MPM effectively suppress interference from anomalous targets during background reconstruction, thereby enhancing the background modeling capability. Furthermore, the proposed algorithm detects two small aircraft with greater clarity than traditional methods like GRX and LRX as well as autoencoder-based models such as RGAE and GAED, indicating that TAMP-Net possesses strong adaptability to multi-scale targets.

TABLE I
COMPARISON OF AUC FOR DIFFERENT ALGORITHMS ON THREE DATASETS.

Method	Salinas	HYDICE	Gulfport
RX [7]	0.80742	0.98482	0.95260
CRD [8]	0.99542	0.98190	0.94131
LRASR [9]	0.92741	0.97927	0.96247
LSDM-Mog [26]	0.60313	0.97963	0.92554
BS^{3}LNet [17]	0.99669	0.97064	0.94917
STAD [27]	0.92234	0.92523	0.94748
NL2Net [18]	0.98934	0.98471	0.98853
Ours	**0.99685**	**0.98643**	**0.99320**

As reflected in Fig. 5, the logarithmic ROC curves clearly highlight TAMP-Net's advantage over competing methods, especially in the low false alarm rate region, validating its robustness and practical applicability. Table I and Fig. 5 show that the proposed TAMP-Net achieves excellent detection performance across multiple datasets, with high AUC scores maintained on all datasets, demonstrating strong generalization capability and stability. On the Gulfport dataset, our method achieved an AUC of 0.99320, outperforming the second-best method (0.96247) by approximately 0.03. The superior performance on the Gulfport dataset can be attributed to TAMP-Net's ability to effectively mitigate the influence of small-scale anomalies during background reconstruction. These results confirm the effectiveness of the entire strategy.

E. Ablation Study

To assess the contribution of each component in the TAMP-Net, we conducted a series of ablation experiments by progressively adding the TARM and the MPM. It is worth noting that since pre-detection is to provide abnormal target positions to TARM, the pre-detection module is also removed when TARM is not employed.

Table II presents the AUC scores on the Salinas dataset under different module configurations. As shown, the model performance is notably improved when either TARM or MPM is incorporated individually, with the most remarkable performance boost observed when TARM is added alone. This underscores the pivotal role of target replacement in mitigating target interference. Overall, these results provide strong evidence for the effectiveness and necessity of each component within the TAMP-Net.

Furthermore, the ablation results also reflect the differentiated value of each module. Introducing TARM alone yields a significant improvement by further suppressing missed anomalies and enhancing the robustness of background modeling. Although the performance gain from MPM is relatively modest compared to TARM, its high masking ratio (up to 90%) can reduce the inference cost by approximately 80% compared with the basic autoencoder network without masking. This efficiency advantage is particularly critical for practical HAD tasks with large data volumes. Therefore, MPM possesses significant and non-negligible practical reference value beyond pure performance enhancement.

TABLE II
ABLATION ON SALINAS DATASET.

TARM	MPM	AUC
-	-	0.92023
-	√	0.94457
√	-	0.99624
√	√	**0.99685**

IV. CONCLUSION

To address the impact of anomalous targets on background reconstruction, we propose TAMP-Net for HAD. TARM is capable of detecting and suppressing significant anomalies, thereby minimizing interference to background estimation and providing a clearer initial background. Subsequently, the MPM mitigates the adverse impact of missed targets by employing a masking strategy, thereby further purifying the background. Qualitative and quantitative results on three datasets confirm the superiority of the TAMP-Net.

Future research will advance the model's architecture for better generalization and scene adaptability, alongside developing self-adaptive parameter mechanisms to boost detection accuracy and robustness.

REFERENCES

[1] Hongjun Su, Zhaoyue Wu, Huihui Zhang, and Qian Du, "Hyperspectral anomaly detection: A survey," IEEE Geoscience and Remote Sensing Magazine, vol. 10, no. 1, p.64-90, 2022.

[2] Zebin Wu, Jin Sun, Yi Zhang, Yaogin Zhu, Jun Li, Antonio Plaza, Jón Atli Benediktsson, and Zhihui Wei, "Scheduling-guided automatic processing of massive hyperspectral Image Classification on Cloud Computing Architectures," IEEE Transactions on Cybernetics, vol.51, no. 7, P.3588-3601, 2021.

[3] Zhou Zhang and Degang Wang, Xu Sun, Lina Zhuang, Rong Liu, and Ni Li, "Spatial sampling and grouping information entropy strategy based on kernel fuzzy c-means clustering method for hyperspectral band selection," Remote Sensing, vol. 14, no. 19, 2022.

[4] Weiqiang Rao, Lianru Gao, Ying Qu, Xu Sun, Bing Zhang, and Jocelyn Chanussot, "Siamese transformer network for hyperspectral image target detection," IEEE Transactions on Geoscience and Remote Sensing, vol. 60, pp. 1–19, 2022.

[5] Bing Lu, Phuong D. Dao, Jiangui Liu, Yuhong He, and Jiali Shang, "Recent advances of hyperspectral imaging technology and applications in agriculture," Remote Sensing, vol. 12, no. 16, 2020.

[6] Degang Wang, Lianru Gao, Ying Qu, Xu Sun, and Wenzhi Liao, "Frequency-to-spectrum mapping gan for semisupervised hyperspectral anomaly detection," CAAI Transactions on Intelligence Technology, vol. 8, no. 4, pp. 1258–1273, Jan. 2023.

[7] Chein-I Chang, "Target-to-anomaly conversion for hy perspectral anomaly detection," IEEE Transactions on Geoscience and Remote Sensing, vol. 60, pp. 1–28, 2022.

[8] Wei Li and Qian Du, "Collaborative representation for hyperspectral anomaly detection," IEEE Transactions on Geoscience and Remote Sensing, vol. 53, no. 3, pp. 1463–1474, 2015.

[9] Yang Xu, Zebin Wu, Jun Li, Antonio Plaza, and Zhihui Wei, "Anomaly detection in hyperspectral images based on low-rank and sparse representation," IEEE Transactions on Geoscience and Remote Sensing, vol. 54, no. 4, pp. 1990–2000, 2016.

[10] W. Li, G. Wu, and Q. Du, "Transferred deep learning for anomaly detection in hyperspectral imagery," IEEE Transactions on Geoscience and Remote Sensing, Lett.,vol. 14, no. 5, pp. 597-601, May 2017.

[11] Y. Huo, X. Cheng, S. Lin, M. Zhang, and H. Wang, "Memory-augmented autoencoder with adaptive reconstruction and sample attribution mining for hyperspectral anomaly detection," IEEE Trans. Geosci. Remote Sens.,vol. 62, 2024, Art. no. 5518118.

[12] K. Jiang, W. Xie, J. Lei, T. Jiang, and Y. Li, "LREN: Low-rank embedded network for sample-free hyperspectral anomaly detection," in Proc. AAAl Conf. Artif. Intell., 2021, vol. 35, no. 5, pp. 4139-4146.

[13] J. Wang, S. Guo, Z. Hua, R. Huang, J. Hu, and M. Gong, "CL-CaGAN:Capsule differential adversarial continual learning for cross-domain hyperspectral anomaly detection,"IEEE Transactions on Geoscience and Remote Sensing,vol. 62.2024. Art. no. 5517315

[14] E. Bati, A. Caliskan, A. Koz, and A. A. Alatan, "Hyperspectral anomaly detection method based on auto-encoder," Proc. SPIE, vol. 9643,Oct. 2015. Art. no. 96430N.

[15] G. E. Hinton and R. Zemel, "Autoencoders, minimum description lengthand Helmholtz free energy," in Proc. Adv. Neural Inf. Process. Syst.,vol. 6, 1993, pp. 3-10.

[16] S. Chang, B. Du, and L. Zhang, "A sparse autoencoder based hyperspectral anomaly detection algorihtm using residual of reconstruction error," in Proc. 1GARSS, Jul. 2019,pp. 5488-5491.

[17] Lianru Gao, Degang Wang, Lina Zhuang, Xu Sun, Min Huang, and Antonio Plaza, "Bs3lnet: A new blind spot self-supervised learning network for hyperspectral anomaly detection," IEEE Transactions on Geoscience and Remote Sensing, vol. 61, pp. 1–18, 2023.

[18] D. Wang, L. Ren, X. Sun, L. Gao and J. Chanussot, "Nonlocal and Local Feature-Coupled Self-Supervised Network for Hyperspectral Anomaly Detection," in IEEE Journal of Selected Topics in Applied Earth Observations and Remote Sensing, vol. 18, pp. 6981-6993, 2025.

[19] J. Kim, S. Kim,J.Lee, K.Yoo, andS.Byun, "Crnsim: A new similarity index capturing global and local spectral differences in hyperspectral data," USA, 2025, vol. 3 of AHFE Open Access, AHFE International.

[20] Vishnu, S., Nidamanuri, R. R., and Bremananth, R. Spectral material mapping using hyperspectral imagery: A review of spectral matching and library search methods, Geocarto International Volume 28, No. 2, 2013.

[21] Yingzhao Shao, Yunsong Li, Li Li, Yuanle Wang, Yuchen Yang, Yueli Ding, Mingming Zhang, Yang Liu, and Xiangqiang Gao, "Ranet: Relationship attention for hyperspectral anomaly detection," Remote Sensing, vol. 15, no. 23, 2023.

[22] Huan Liu, Wei Li, Wen Jia, Hong Sun, Mengmeng Zhang, Lujie Song, and Yuanyuan Gui, "Clusterformer for pine tree disease identification based on uav remote sensing image segmentation," IEEE Transactions on Geoscience and Remote Sensing, vol. 62, 2024.

[23] Jun Li and Jose M. Bioucas-Dias, "Minimum vol ume simplex analysis: A fast algorithm to unmix hyperspectral data," in IGARSS 2008- 2008

IEEE International Geoscience and Remote Sensing Symposium, 2008, vol. 3, pp. 250–253.
[24] Jingtao Li, Xinyu Wang, Shaoyu Wang, Hengwei Zhao, andYanfei Zhong, “One-stepdetection paradigm for hy perspectral anomaly detection via spectral deviation re lationship learning,” IEEE Transactions on Geoscience and Remote Sensing, vol. 62, pp. 1–15, 2024.
[25] Xudong Kang, Xiangping Zhang, Shutao Li, Kenli Li, Jun Li, and Jón Atli Benediktsson, “Hyperspectral anomaly detection with attribute and edge-preserving f ilters,” IEEE Transactions on Geoscience and Remote Sensing, vol. 55, no. 10, pp. 5600–5611, 2017.
[26] Lu Li, Wei Li, Qian Du, and Ran Tao, “Low-rank and sparse decomposition with mixture of gaussian for hy perspectral anomaly detection,” IEEE Transactions on Cybernetics, vol. 51, no. 9, pp. 4363–4372, 2021.
[27] Jitao Ma, Weiying Xie, and Yunsong Li, “Exploring hyperspectral anomaly detection with human vision: A small target aware detector,” Neural Networks, vol. 184, Apr 2025
[28] C.-I. Chang. C.-Y. Lin, P.-C. Chung, and P. F. Hu, “Iterativespectral-spatial hyperspectral anomaly detection,” IEEE Transactions on Geoscience and Remote Sensing, vol. 61, 2023, Art. no. 5504330.